

# Fe-doping effects on the structural and electrochemical properties of $0.5\text{Li}_2\text{MnO}_3 \cdot 0.5\text{LiMn}_{0.5}\text{Ni}_{0.5}\text{O}_2$ electrode material

F. Lian · M. Gao · W. H. Qiu · P. Axmann ·  
M. Wohlfahrt-Mehrens

Received: 27 February 2012 / Accepted: 9 April 2012 / Published online: 26 April 2012  
© Springer Science+Business Media B.V. 2012

**Abstract** With the aim of achieving a high-performance  $0.5\text{Li}_2\text{MnO}_3 \cdot 0.5\text{LiMn}_{0.5}\text{Ni}_{0.5}\text{O}_2$  material, a series of  $0.5\text{Li}_2\text{MnO}_3 \cdot 0.5\text{LiMn}_x\text{Ni}_y\text{Fe}_{(1-x-y)}\text{O}_2$  ( $0.3 \leq x \leq 0.5$ ,  $0.4 \leq y \leq 0.5$ ) samples with low Fe content was synthesized via coprecipitation of carbonates. Its crystal structure and electrochemical performance were characterized by means of powder X-ray diffraction, field emission scanning electron microscopy, X-ray photoelectron spectroscopy, galvanostatic charge/discharge testing, cyclic voltammetry, and electrochemical impedance spectra. Rietveld refinements with a model integrating  $R\bar{3}m$  and  $Fm\bar{3}m$  indicate that a low concentration of Fe incorporated in  $0.5\text{Li}_2\text{MnO}_3 \cdot 0.5\text{LiMn}_{0.5}\text{Ni}_{0.5}\text{O}_2$  decrease a disordered cubic domain of the composite structure. The preferential distribution of Fe in cubic rock-salt contributes to an unimaginable decrease of *c*-axis parameter of the predominant layered structure as the Fe content increases. Moreover, including Fe as a dopant can kinetically improve crystallization and also change the ratio of  $\text{Mn}^{3+}/\text{Mn}^{4+}$  and  $\text{Ni}^{3+}/\text{Ni}^{2+}$ . As a result,  $0.5\text{Li}_2\text{MnO}_3 \cdot 0.5\text{LiMn}_{0.4}\text{Ni}_{0.5}\text{Fe}_{0.1}\text{O}_2$  exhibits lower Warburg impedance and higher reversible capacity than the undoped material.

**Keywords** Li-ion battery · Electrochemical property · Doping

## 1 Introduction

Recently,  $x\text{Li}_2\text{MnO}_3 \cdot (1-x)\text{LiMO}_2$  ( $M = \text{Ni}$  and  $\text{Mn}$ , etc.,  $0 < x < 1$ ) solid solutions have been considered as a promising substitute for commercial  $\text{LiCoO}_2$  because of its higher capacity, better stability, safer behavior, and cheaper raw materials [1, 2].  $\text{Li}_2\text{MnO}_3$  integrated into a  $\text{LiMO}_2$  matrix not only prevents structural collapse of the layered materials at low Li content, but also can be activated to deliver capacity at high voltage [3, 4]. Elements such as  $\text{Co}^{3+}$  [5],  $\text{Al}^{3+}$  [6], and  $\text{Cr}^{3+}$  [7] have been doped into the series in attempts to improve its cycling stability and/or rate capability. A first principle calculation indicated that the mobility of Li in layered materials mainly depends on the transition metal species, and that including Fe with a large radius ( $r_{\text{Fe}^{3+}} = 0.64 \text{ \AA}$ ) as a dopant can broaden the Li–O interslab distance and thus decrease the energy barrier for Li hopping [8]. Moreover, introduction of iron can also reduce the cost of the electrode material due to its abundance. Our studies have focused on Fe-substituted series, with the aim of achieving a high-performance cathode material that can be produced cheaply. However,  $\text{Li}_2\text{MnO}_3$ -based material with high Fe content above 20 % showed the obvious coexisting phase of layered ( $R\bar{3}m$ ) and cubic ( $Fm\bar{3}m$ ) rock-salt as reported by Tabuchi et al. [9, 10]. In addition, Kikkawa et al. [11] found that an integrated structure led to an inhomogeneous intralayer distribution of multiple transition metal ions and a large capacity fading during the subsequent cycles [12, 13]. The previous studies suggested that appropriate Fe content is critical to improve the structural and electrochemical properties of  $x\text{Li}_2\text{MnO}_3 \cdot (1-x)\text{LiMO}_2$  solid solution. So our studies have focused on  $0.5\text{Li}_2\text{MnO}_3 \cdot 0.5\text{LiMn}_{0.5}\text{Ni}_{0.5}\text{O}_2$  with low Fe content, its crystal structure and electrochemical performance are

F. Lian (✉) · M. Gao · W. H. Qiu  
School of Materials Science and Engineering, University of  
Science and Technology Beijing, Beijing 100083, China  
e-mail: lianfang@mater.ustb.edu.cn

P. Axmann · M. Wohlfahrt-Mehrens  
Centre of Solar Energy and Hydrogen Research Baden-  
Württemberg, Helmholtzstr. 8, 89081 Ulm, Germany

characterized by means of powder X-ray diffraction (XRD), field emission scanning electron microscopy (FESEM), inductively coupled plasma optical emission spectroscopy (ICP-OES), X-ray photoelectron spectroscopy (XPS), galvanostatic charge/discharge testing, cyclic voltammetry (CV), and electrochemical impedance spectra (EIS). Moreover, the material with  $\text{Fe}^{3+}$ -substituted for  $\text{Ni}^{2+}$  and  $\text{Mn}^{4+}$  simultaneously, which is rarely reported to our knowledge, is also designed and studied considering the charge balance of the system. In our previous study, the coprecipitation of carbonates was responsible for the homogeneous dispersion of Ni and Mn in the precursor, which led to  $\text{LiNi}_{1/2}\text{Mn}_{1/2}\text{O}_2$  with excellent electrochemical performance [14]. As a result,  $0.5\text{Li}_2\text{MnO}_3 \cdot 0.5\text{LiMn}_x\text{Ni}_y\text{Fe}_{(1-x-y)}\text{O}_2$  ( $0.3 \leq x \leq 0.5$ ,  $0.4 \leq y \leq 0.5$ ) samples presented herein are also prepared via coprecipitation of carbonates.

## 2 Experimental

### 2.1 Preparation

$\text{LiOH} \cdot \text{H}_2\text{O}$ ,  $\text{Ni}(\text{NO}_3)_2 \cdot 6\text{H}_2\text{O}$ ,  $\text{Fe}(\text{NO}_3)_3 \cdot 9\text{H}_2\text{O}$  (all are 99.9 % in purity), and  $\text{Mn}(\text{NO}_3)_2$  (50 % aqueous solution) were used as starting materials for  $0.5\text{Li}_2\text{MnO}_3 \cdot 0.5\text{LiMn}_x\text{Ni}_y\text{Fe}_{(1-x-y)}\text{O}_2$  ( $0.3 \leq x \leq 0.5$ ,  $0.4 \leq y \leq 0.5$ ) (samples a–d, as shown in Table 1). A mixed aqueous solution of

transition metal nitrate (2.0 M) and  $\text{Na}_2\text{CO}_3$  solution (2.0 M) were simultaneously added dropwise into a reactor containing vigorously stirring distilled water. The pH in the reactor was maintained at 9, and the temperature was held at 60 °C for 4 h. The resulting precipitates were filtered and washed three times to remove excess  $\text{Na}^+$ , and then dried under nitrogen at 120 °C. The obtained precursor was subsequently mixed with a stoichiometric amount of  $\text{LiOH} \cdot \text{H}_2\text{O}$  by grinding. The mixture was finally sintered at 800 °C for 12 h in air.

### 2.2 Characterization

Powder XRD (Rigaku D/max, Japan) using  $\text{CuK}\alpha$  radiation was used to identify the crystalline phase of the as-prepared samples. Detailed structure testing was carried out with a scanning step of 0.01 and scanning time of 1 s per step. Profile refinement was then performed on the XRD data using the TOPAS software (Version 2.1, Bruker-AXS). FESEM analysis was performed using a Zeiss supra55 field emission scanning electron microscope (Germany). The precise cation composition of the samples was determined by ICP-OES (Varian Vista-MPX CCD Simultaneous ICP-OES, America). XPS of the compounds were obtained using a PHI5300 spectrometer (Perkin-Elmer, America) with monochromatic  $\text{MgK}\alpha$  radiation ( $h\nu = 1253.6$  eV). High resolution spectra were recorded in a constant pass

**Table 1** ICP results and structural characterizations of  $0.5\text{Li}_2\text{MnO}_3 \cdot 0.5\text{LiMn}_x\text{Ni}_y\text{Fe}_{(1-x-y)}\text{O}_2$  samples

Sample	Target composition	Stoichiometry from ICP				Layered rock-salt ( $R\bar{3}m$ ) phase		Cubic rock-salt ( $Fm\bar{3}m$ ) phase		Reliability factor
		Li	Ni	Mn	Fe	Mass fraction (%)	Lattice parameters (Å)	Mass fraction (%)	Lattice parameters (Å)	
a	$0.5\text{Li}_2\text{MnO}_3 \cdot 0.5\text{LiMn}_{0.5}\text{Ni}_{0.5}\text{O}_2$	1.19	0.20	0.61	0	92.0	$a = 2.8585$ , $c = 14.2508$	8.0	4.0875	$R_{\text{wp}} = 7.41$ % $R_{\text{p}} = 5.49$ % $R_{\text{exp}} = 5.21$ % GOF = 1.08
b	$0.5\text{Li}_2\text{MnO}_3 \cdot 0.5\text{LiMn}_{0.4}\text{Ni}_{0.5}\text{Fe}_{0.1}\text{O}_2$	1.18	0.20	0.58	0.04	93.5	$a = 2.8596$ , $c = 14.2684$	6.5	4.0881	$R_{\text{wp}} = 7.48$ % $R_{\text{p}} = 5.66$ % $R_{\text{exp}} = 6.57$ % GOF = 1.09
c	$0.5\text{Li}_2\text{MnO}_3 \cdot 0.5\text{LiMn}_{0.4}\text{Ni}_{0.4}\text{Fe}_{0.2}\text{O}_2$	1.19	0.16	0.59	0.08	91.1	$a = 2.8724$ , $c = 14.2274$	8.9	4.0943	$R_{\text{wp}} = 7.96$ % $R_{\text{p}} = 5.38$ % $R_{\text{exp}} = 5.64$ % GOF = 1.03
d	$0.5\text{Li}_2\text{MnO}_3 \cdot 0.5\text{LiMn}_{0.3}\text{Ni}_{0.4}\text{Fe}_{0.3}\text{O}_2$	1.18	0.16	0.54	0.12	89.6	$a = 2.8659$ , $c = 14.2423$	10.4	4.1218	$R_{\text{wp}} = 7.46$ % $R_{\text{p}} = 5.45$ % $R_{\text{exp}} = 5.85$ % GOF = 1.02

energy mode (20 eV). Charges were referenced against the binding energy (BE) of adventitious carbon (C1s = 284.6 eV) and have associated errors of  $\pm 0.1$  eV. The resulting spectra were analyzed using XPS peak fit software with a Shirley-type background subtracted from the recorded spectra. Curve fitting and deconvolution of overlapped peaks was performed by nonlinear least-square fitting with a Gauss-Lorentz curve (ratio 80:20).

### 2.3 Electrochemical test of the electrodes

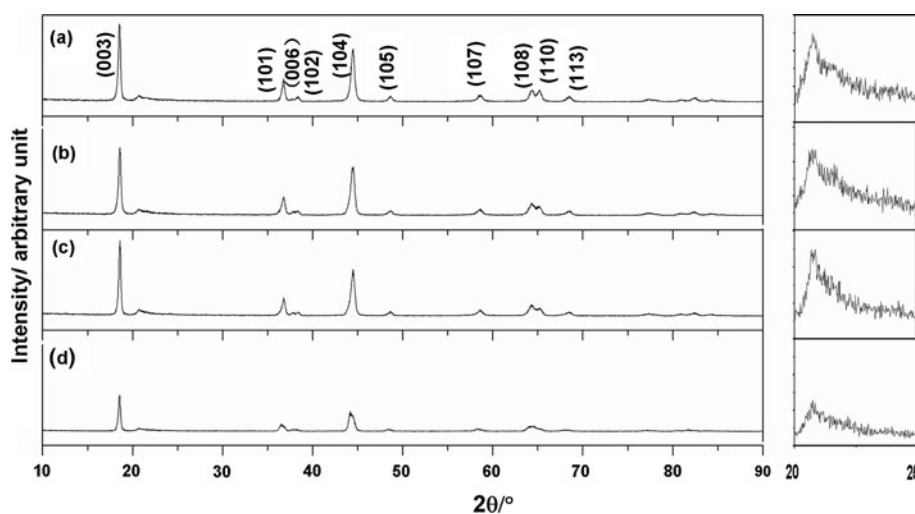
For the electrochemical studies, the positive electrode was fabricated from 85 wt% of the synthesized powder samples as the active material, 10 wt% acetylene black as a conductive additive, and 5 wt% polytetrafluoroethylene as a binder. The mixture was stirred, dried and then rolled into a film with a thickness of 100  $\mu\text{m}$ . The electrode film was dried and degreased under vacuum for 24 h at 120  $^{\circ}\text{C}$  to remove any solvent on the electrode surface. Coin cells (CR2032) containing  $\text{LiPF}_6$  (1 M) dissolved in ethylene carbonate (EC), dimethyl carbonate (DMC), and diethyl carbonate (DEC) in a 1:1:1 volume ratio (Beijing Institute of Chemical Reagents, China) as the electrolyte, and metallic lithium and porous polypropylene films as anode and separator, respectively, were assembled and sealed in an argon-filled glove box. Charge and discharge tests were performed galvanostatically between 2.5 and 4.8 V at room temperature at 0.1 C with a LAND CT2001A battery test system (Jinnuo Wuhan Corp., China). CV was carried out on a CHI660A electrochemical workstation (CH Instrumental, China) between 2.0 and 5.0 V at a scanning rate of 0.1  $\text{mV s}^{-1}$ . EIS was employed to determine the resistance of cycled cells. The tests were performed under a frequency range of 100 kHz–0.01 Hz using a vibration voltage of 10 mV.

## 3 Results and discussion

### 3.1 Crystal structure analysis

ICP results as concluded in Table 1 indicate that the average chemical compositions of the obtained materials are very close to the targeted stoichiometry. Powder XRD data for  $0.5\text{Li}_2\text{MnO}_3 \cdot 0.5\text{LiMn}_x\text{Ni}_y\text{Fe}_{(1-x-y)}\text{O}_2$  ( $0.3 \leq x \leq 0.5$ ,  $0.4 \leq y \leq 0.5$ ) are shown in Fig. 1. The patterns can be indexed based on a  $\alpha\text{-NaFeO}_2$  structure with space group  $R\bar{3}m$ . And the peaks between  $20^{\circ}$  and  $25^{\circ}$  correspond to the superlattice ordering of  $\text{Li}^+$  and  $\text{Mn}^{4+}$  in the transition metal layer [15]. The previous reports suggested that the introduction of Fe into the series lead to the appearance of cubic ( $Fm\bar{3}m$ ) rock-salt [9–11]. But cubic structure  $Fm\bar{3}m$ , which show the subtle difference in main diffraction peaks with  $R\bar{3}m$  cannot be detected from the initial XRD analysis. Rietveld refinement, applied to XRD patterns is an effective technique for local structure analysis [16]. And therefore the samples were analyzed herein in detail by employing the Rietveld refinement with a model integrating  $Fm\bar{3}m$  (No. 225) and  $R\bar{3}m$  (No.166) structure. The refinement patterns of  $0.5\text{Li}_2\text{MnO}_3 \cdot 0.5\text{LiMn}_{0.4}\text{Ni}_{0.4}\text{Fe}_{0.2}\text{O}_2$  sample is shown as an example in Fig. 2, which are in good agreement with the experimental patterns. The calculated structural properties and the reliability factors of refinement are summarized in Table 1. All of  $0.5\text{Li}_2\text{MnO}_3 \cdot 0.5\text{LiMn}_x\text{Ni}_y\text{Fe}_{(1-x-y)}\text{O}_2$  ( $0.3 \leq x \leq 0.5$ ,  $0.4 \leq y \leq 0.5$ ) samples can be assigned as a composite structure consisting of a predominant layered ( $R\bar{3}m$ ) phase and a small amount of cubic rock-salt ( $Fm\bar{3}m$ ).  $0.5\text{Li}_2\text{MnO}_3 \cdot 0.5\text{LiMn}_{0.3}\text{Ni}_{0.4}\text{Fe}_{0.3}\text{O}_2$  samples with high Fe content exhibit the largest proportion of cubic rock-salt about 10.4 %. While  $0.5\text{Li}_2\text{MnO}_3 \cdot 0.5\text{LiMn}_{0.4}\text{Ni}_{0.5}\text{Fe}_{0.1}\text{O}_2$  includes 6.5 % cubic structure and 93.5 % layered one, which shows the lower

**Fig. 1** XRD patterns of  $0.5\text{Li}_2\text{MnO}_3 \cdot 0.5\text{LiMn}_x\text{Ni}_y\text{Fe}_{(1-x-y)}\text{O}_2$  samples



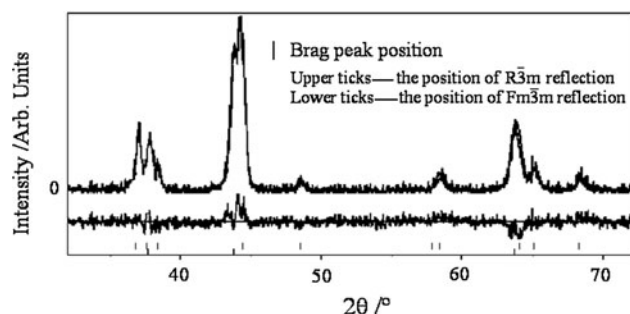


**Fig. 2** Rietveld refinement of  $0.5\text{Li}_2\text{MnO}_3 \cdot 0.5\text{LiMn}_{0.4}\text{Ni}_{0.4}\text{Fe}_{0.2}\text{O}_2$  material using a model integrating cubic rock-salts ( $Fm \bar{3}m$ ) and layered ones ( $R \bar{3}m$ )

proportion of cubic rock-salt than the undoped  $0.5\text{Li}_2\text{MnO}_3 \cdot 0.5\text{LiMn}_{0.5}\text{Ni}_{0.5}\text{O}_2$  samples. Like the previous reports on  $x\text{Li}_2\text{MnO}_3 \cdot (1-x)\text{LiMO}_2$  solid solution, the phase composition show dependence on the content of Fe dopant. The samples with high Fe content above 20 % showed the obvious coexisting phase of layered ( $R \bar{3}m$ ) and cubic ( $Fm \bar{3}m$ ) rock-salt [9–11], while no observable cubic phase was detected from initial XRD analysis for the samples with low Fe content. In addition, the prepare method also contributes to the appearance of the composite structure such as  $R \bar{3}m$  and  $Fm \bar{3}$  in the solid solution, our observations from three batches of  $0.5\text{Li}_2\text{MnO}_3 \cdot 0.5\text{LiMn}_{0.4}\text{Ni}_{0.5}\text{Fe}_{0.1}\text{O}_2$  samples indicate that a low concentration of Fe-doping can decrease the cubic domain in  $0.5\text{Li}_2\text{MnO}_3 \cdot 0.5\text{LiMn}_{0.5}\text{Ni}_{0.5}\text{O}_2$  material.

Furthermore, it is found from the rietveld refinement that the lattice constant of the predominant layered phase fluctuates with an increase of Fe content. Incorporation of a small amount of  $\text{Fe}^{3+}$  replacing  $\text{Mn}^{4+}$  ions ( $\gamma_{\text{Mn}^{4+}} = 0.52 \text{ \AA}$ ,  $\gamma_{\text{Fe}^{3+}} = 0.64 \text{ \AA}$ ) contributes to slightly larger  $c$ -axis of the layered structure and larger lattice parameter of the cubic rock-salt for  $0.5\text{Li}_2\text{MnO}_3 \cdot 0.5\text{LiMn}_{0.4}\text{Ni}_{0.5}\text{Fe}_{0.1}\text{O}_2$ . However,  $0.5\text{Li}_2\text{MnO}_3 \cdot 0.5\text{LiMn}_{0.4}\text{Ni}_{0.4}\text{Fe}_{0.2}\text{O}_2$  shows an continuous increasing lattice parameter of  $Fm \bar{3}m$  phase and a reduced  $c$ -axis value of the layered structure as the Fe content increases, while  $0.5\text{Li}_2\text{MnO}_3 \cdot 0.5\text{LiMn}_{0.3}\text{Ni}_{0.4}\text{Fe}_{0.3}\text{O}_2$  exhibit smaller  $c$ -axis of the layered structure compared with  $0.5\text{Li}_2\text{MnO}_3 \cdot 0.5\text{LiMn}_{0.4}\text{Ni}_{0.4}\text{Fe}_{0.2}\text{O}_2$ . Change in lattice constant of the composite structure indicates a preferential distribution of Fe in cubic rock-salt, which is in agreement with the previous reports that layered ( $R \bar{3}m$ ) and cubic ( $Fm \bar{3}m$ ) phase of the series with high Fe content were assigned as Fe-substituted  $\text{Li}_2\text{MnO}_3$  and Mn-substituted  $\text{LiFeO}_2$ , respectively [11]. However, the occupation ratios of Fe cannot be determined due to the low concentration of Fe dopant and the limitation of analyse method. So the composite structure of the as-obtained material, in which Fe cations energetically prefer the occupation in the cubic rock-salt,

should be considered to completely understand the Fe-doping effects on the crystal structure and electrochemical performance of  $0.5\text{Li}_2\text{MnO}_3 \cdot 0.5\text{LiMn}_{0.5}\text{Ni}_{0.5}\text{O}_2$ .

Crystallite size is also calculated according to Scherrer equation as the formula (1).

$$D = K\lambda / \beta \cos \theta \quad (1)$$

where  $K$  is the Scherrer constant (0.89 for integral breadth of spherical crystals w/cubic symmetry),  $\lambda$  is the wavelength,  $\theta$  is the diffraction angle, and  $\beta$  is the full width at half maximum (FWHM). The mean crystallite size of the sample A, B, C, and D were determined to be 11.8, 12.2, 14.1, and 17.6 nm, responsibility.

### 3.2 Morphology

Scanning electron micrographs (SEM) images obtained for the  $0.5\text{Li}_2\text{MnO}_3 \cdot 0.5\text{LiMn}_x\text{Ni}_y\text{Fe}_{(1-x-y)}\text{O}_2$  powders are shown in Fig. 3. The particles in the  $0.5\text{Li}_2\text{MnO}_3 \cdot 0.5\text{LiMn}_{0.5}\text{Ni}_{0.5}\text{O}_2$  sample exhibit a homogenous morphology, with diameters of around 150–200 nm. The size of the particles in the samples increases as the content of Fe increases;  $0.5\text{Li}_2\text{MnO}_3 \cdot 0.5\text{LiMn}_{0.3}\text{Ni}_{0.4}\text{Fe}_{0.3}\text{O}_2$  consists of crystallites of around 300 nm in diameter. The results show that the particles and crystallites become large with an increase of Fe content in the materials. This indicates that adding Fe as a dopant can kinetically improve crystallization.

### 3.3 Oxidation states of the transition metal ions

Figure 4a, b show the Ni and Mn XPS core spectra for the sample A, B, C, and D, while Fig. 4c demonstrates the Fe XPS core spectra for the sample B, C, and D. In the Ni XPS spectra, a characteristic satellite peak around 860.3 eV is also noted in addition to the  $\text{Ni}(2p_{3/2})$  peak. Such a satellite peak is also observed in  $\text{Li}(\text{Ni}_{1/3}\text{Co}_{1/3}\text{Mn}_{1/3})\text{O}_2$  and is explained as due to the multiple splitting in the energy level of the Ni-containing oxides [17]. The best fit for the  $\text{Ni}(2p_{3/2})$  spectrum gives two BE values. The major peak with a BE = 854.0 eV and a less prominent one at 855.5 eV are in agreement with those reported for  $\text{Ni}^{3+}$  in  $\text{LiMn}_{1.5}\text{Ni}_{0.5}\text{O}_4$  and  $\text{Ni}^{3+}$  in  $\text{LiNiO}_2$ , respectively. The deconvolution of the  $\text{Mn}(2p_{3/2})$  spectrum also gives two BEs for its best fit. Comparing our BEs with the values reported for  $\text{Li}(\text{Ni}_{1/3}\text{Co}_{1/3}\text{Mn}_{1/3})\text{O}_2$ , we note that the major peak centered at 642.2 eV corresponds to  $\text{Mn}^{4+}$  and the minor one at 641.0 eV corresponds to  $\text{Mn}^{3+}$  ions in the compound. The  $\text{Fe}(2p_{3/2})$  spectra of all of the Fe-doped materials exhibit double-peaks with BE of  $\sim 711$  and  $\sim 709$  eV (Fig. 4c), which can be attributed to  $\text{Fe}^{3+}$  (Fig. 4c). The XPS spectra show that the predominant oxidation states of Ni and Mn in the undoped materials are 2+ and 4+, respectively. A minor contribution from  $\text{Ni}^{3+}$  and



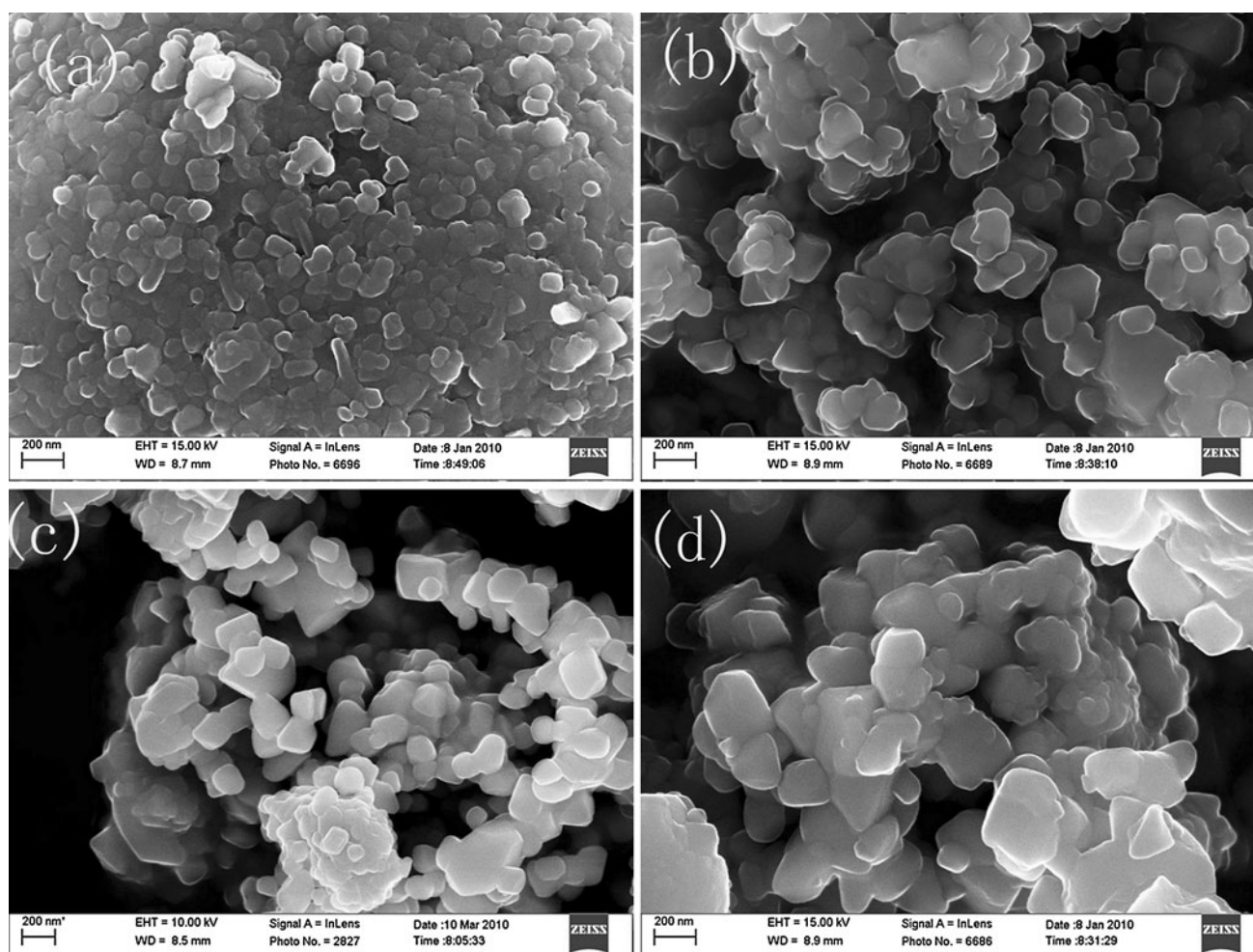


**Fig. 3** SEM images of  $0.5\text{Li}_2\text{MnO}_3 \cdot 0.5\text{LiMn}_x\text{Ni}_y\text{Fe}_{(1-x-y)}\text{O}_2$  samples

$\text{Mn}^{3+}$  may be caused by a small amount of valence degeneracy through the dynamic equilibrium,  $\text{Ni}^{2+} + \text{Mn}^{4+} \leftrightarrow \text{Ni}^{3+} + \text{Mn}^{3+}$  [18]. Compared with the other samples, the ratio of  $\text{Mn}^{3+}/\text{Mn}^{4+}$  and  $\text{Ni}^{3+}/\text{Ni}^{2+}$  decreases in  $0.5\text{Li}_2\text{MnO}_3 \cdot 0.5\text{LiMn}_{0.4}\text{Ni}_{0.5}\text{Fe}_{0.1}\text{O}_2$ . Furthermore, no variation in the XPS core level spectra of Mn and Ni is detected between  $0.5\text{Li}_2\text{MnO}_3 \cdot 0.5\text{LiMn}_{0.4}\text{Ni}_{0.4}\text{Fe}_{0.2}\text{O}_2$  and the undoped material. The observations suggest that  $0.5\text{Li}_2\text{MnO}_3 \cdot 0.5\text{LiMn}_{0.4}\text{Ni}_{0.4}\text{Fe}_{0.2}\text{O}_2$  maintains charge balance when 0.1 M Mn and 0.1 M Ni are substituted with 0.2 M of Fe. In contrast, the ratio of  $\text{Mn}^{3+}/\text{Mn}^{4+}$  and  $\text{Ni}^{3+}/\text{Ni}^{2+}$  increases in  $0.5\text{Li}_2\text{MnO}_3 \cdot 0.5\text{LiMn}_{0.3}\text{Ni}_{0.4}\text{Fe}_{0.3}\text{O}_2$  samples.

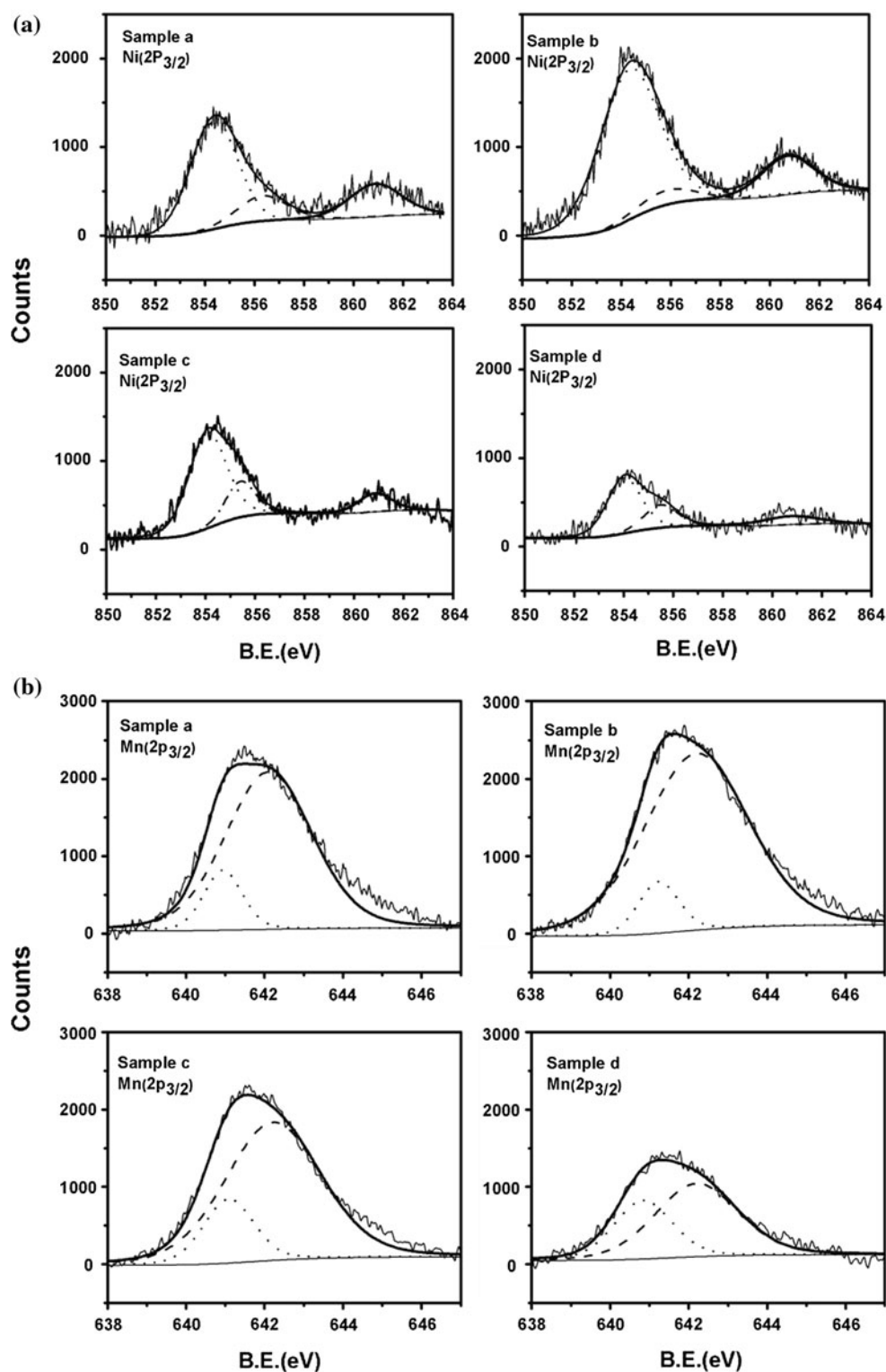
### 3.4 Electrochemical analysis

The charge/discharge voltage curves for the  $\text{Li}/0.5\text{Li}_2\text{MnO}_3 \cdot 0.5\text{LiMn}_x\text{Ni}_y\text{Fe}_{(1-x-y)}\text{O}_2$  cells cycled between 2.5 and 4.8 V are shown in Fig. 5. During the initial charging to 4.8 V, the electrochemical reaction occurs in two main stages: a regular increase in voltage, which is attributed to

the removal of lithium from the electrode material accompanied with the oxidation of  $\text{Ni}^{2+}$  to  $\text{Ni}^{4+}$ , and a voltage plateau above 4.5 V, which could be ascribed to the removal of  $\text{Li}_2\text{O}$  from the structure. With increasing Fe content, cells a, b, c, and d exhibit specific charge capacities of about 232, 241.4, 262.1, and 249.1  $\text{mAh g}^{-1}$ , respectively. Samples a, b, and c deliver similar initial discharge capacities of about 160  $\text{mAh g}^{-1}$ , while sample d shows an initial discharge capacity of 110  $\text{mAh g}^{-1}$ . Moreover, the capacity of samples a, b, and c increases with the cycle number (as shown in Fig. 6).  $0.5\text{Li}_2\text{MnO}_3 \cdot 0.5\text{LiMn}_{0.4}\text{Ni}_{0.5}\text{Fe}_{0.1}\text{O}_2$  electrode requires  $\sim 20$  break-in cycles before a steady capacity of  $\sim 210 \text{ mAh g}^{-1}$  is obtained [19], which is different from the phenomena of severe capacity deterioration of the material with obvious coexisting phase [11]. CV and EIS experiments were also performed to gain insight into the influence of Fe-doping on  $0.5\text{Li}_2\text{MnO}_3 \cdot 0.5\text{LiMn}_{0.5}\text{Ni}_{0.5}\text{O}_2$ .

CV curves obtained for the  $0.5\text{Li}_2\text{MnO}_3 \cdot 0.5\text{LiMn}_x\text{Ni}_y\text{Fe}_{(1-x-y)}\text{O}_2$  ( $0.3 \leq x \leq 0.5$ ,  $0.4 \leq y \leq 0.5$ ) electrodes

**Fig. 4** XPS core level spectra of Mn, Ni, and Fe in  $0.5\text{Li}_2\text{MnO}_3 \cdot 0.5\text{LiMn}_x\text{Ni}_y\text{Fe}_{(1-x-y)}\text{O}_2$  samples



between 2.0 and 5.0 V at a rate of  $0.1 \text{ mV s}^{-1}$  are shown in Fig. 7. During the first charging of the  $\text{Li}/0.5\text{Li}_2\text{MnO}_3 \cdot 0.5\text{LiMn}_{0.5}\text{Ni}_{0.5}\text{O}_2$  cell, there are two oxidation peaks around 4.0 V denoted 1 and 2, respectively [20]. The CV obtained using the  $0.5\text{Li}_2\text{MnO}_3 \cdot 0.5\text{LiMn}_{0.4}\text{Ni}_{0.5}\text{Fe}_{0.1}\text{O}_2$  electrode only exhibits one broad peak near 4.0 V, which

may result from the lower intensity of lithium clustering due to Fe-doping. Although samples a–c show a large irreversible peak starting at 4.45 V, the onset of the irreversible peak shifts to 4.69 V for  $0.5\text{Li}_2\text{MnO}_3 \cdot 0.5\text{LiMn}_{0.3}\text{Ni}_{0.4}\text{Fe}_{0.3}\text{O}_2$ , which suggests that increasing the concentration of Fe will hinder the deintercalation of LiO from the

Fig. 4 continued

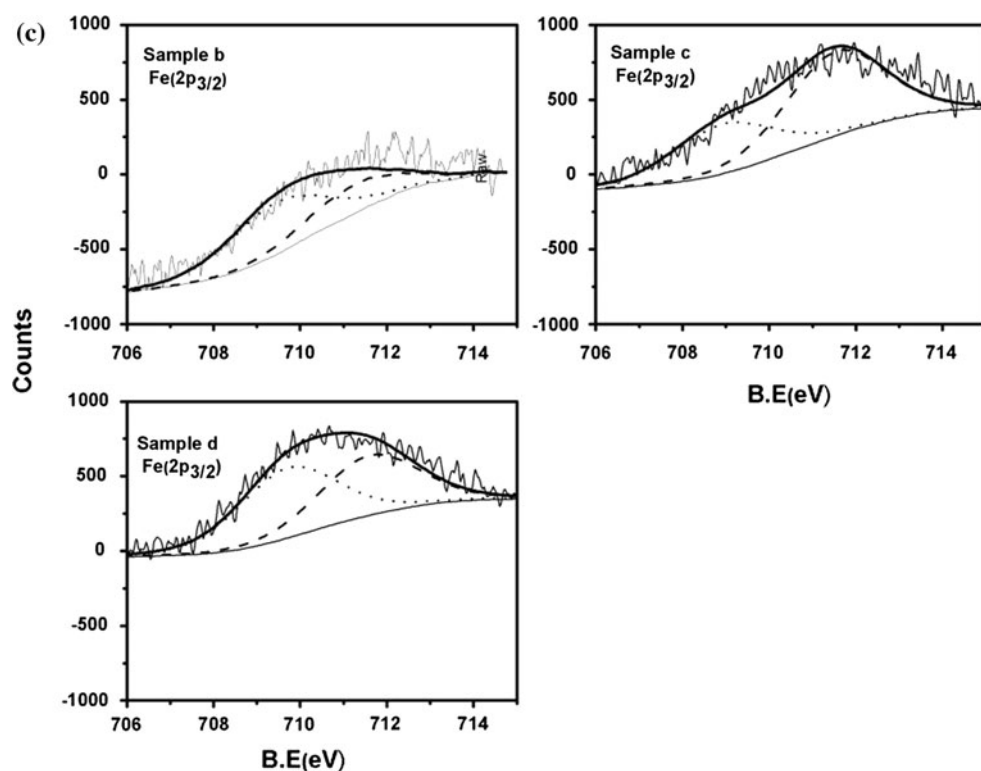


**Fig. 5** Charge/discharge voltage curves obtained for  $\text{Li}/0.5\text{Li}_2\text{MnO}_3\cdot 0.5\text{LiMn}_x\text{Ni}_y\text{Fe}_{(1-x-y)}\text{O}_2$  cells

layered structure at a high potential. The reduction peaks (denoted 1' and 2', normally near 4 V) of sample d during the first discharge also move to higher voltage compared

with the other samples. In addition, the magnitude of two redox peaks at 3.2 V (denoted 3 and 3'), appearing after the electrochemically activation process upon the initial

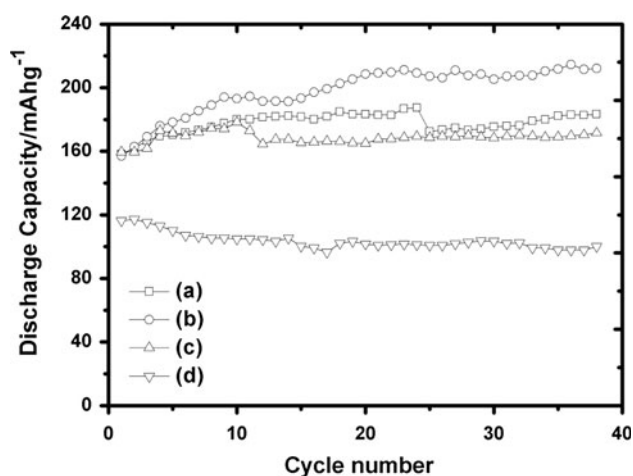


**Fig. 6** Cyclic performance of Li/0.5Li<sub>2</sub>MnO<sub>3</sub>·0.5LiMn<sub>x</sub>Ni<sub>y</sub>Fe<sub>(1-x-y)</sub>O<sub>2</sub> cells

cycling of solid solutions, become smaller for 0.5Li<sub>2</sub>MnO<sub>3</sub>·0.5LiMn<sub>0.3</sub>Ni<sub>0.4</sub>Fe<sub>0.3</sub>O<sub>2</sub>, which demonstrates a decrease of reversible capacity of the material with the increase of Fe content.

Before EIS testing, the electrodes underwent five galvanostatic cycles between 2.5 and 4.8 V and were then charged for 4 h to ensure the stability of the solid electrolyte interface film and its good contact with the electrolyte on the surface of electrode. The corresponding Nyquist plots were given in Fig. 8. The diffusion coefficient of lithium ions,  $D_{Li}$ , can be obtained from analysis of the Warburg impedance,  $Z_W$ , which is expressed in a complex plane as follows [21, 22]:

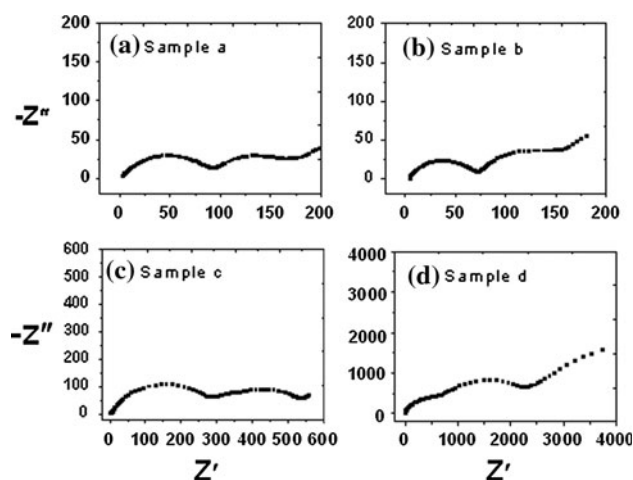


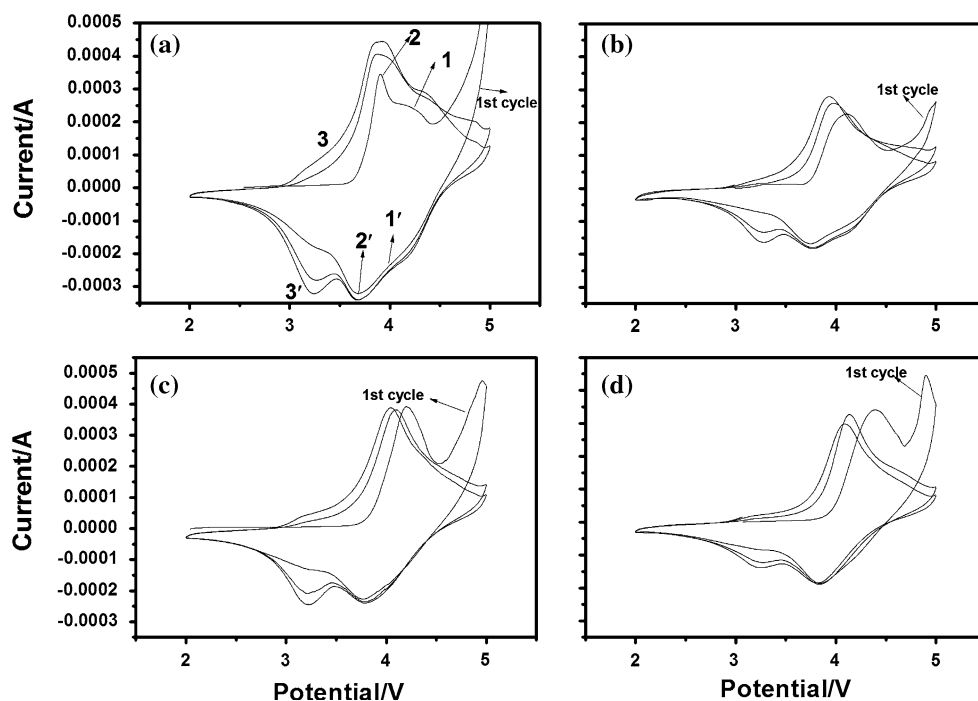
**Fig. 8** EIS of 0.5Li<sub>2</sub>MnO<sub>3</sub>·0.5LiMn<sub>x</sub>Ni<sub>y</sub>Fe<sub>(1-x-y)</sub>O<sub>2</sub> samples

$$Z_{re} = A - \sigma \omega^{-1/2} \quad (2)$$

$$D_{Li} = R^2 T^2 / 2 S^2 n^4 F^4 C^2 \sigma^2 \quad (3)$$

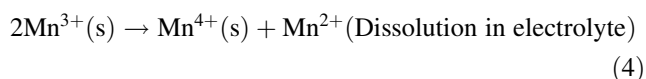
where  $R$  is the gas constant,  $T$  is the absolute temperature,  $S$  is the surface area of the cathode,  $n$  is the number of electrons involved in the reaction ( $n = 1$ ),  $F$  is the Faraday constant,  $C$  is the concentration of lithium ions (in form of mol/mL), and  $\sigma$  is the Warburg factor.  $\sigma$  can be obtained from the slope of the real resistance ( $Z_{re}$ ) versus the inverse square root of the angular frequency ( $\omega^{-1/2}$ ). The lithium diffusion coefficients of samples a, b, c, and d are calculated to be  $9.49 \times 10^{-13}$ ,  $1.24 \times 10^{-12}$ ,  $3.90 \times 10^{-13}$ , and  $3.92 \times 10^{-16} \text{ cm}^2 \text{ s}^{-1}$ , respectively.

**Fig. 7** Cycle voltammograms obtained for Li/0.5Li<sub>2</sub>MnO<sub>3</sub>·0.5LiMn<sub>x</sub>Ni<sub>y</sub>Fe<sub>(1-x-y)</sub>O<sub>2</sub> cells between 2.0 and 5.0 V





The results from EIS of cycled cells is credible to compare the varieties of lithium mobility between the samples. But EIS using three-electrode system, other method such as GITT and PITT are better choices to obtain a more precise diffusion coefficients.  $0.5\text{Li}_2\text{MnO}_3 \cdot 0.5\text{LiMn}_{0.4}\text{Ni}_{0.5}\text{Fe}_{0.1}\text{O}_2$  exhibits high  $\text{Li}^+$  diffusion coefficient, which is contributed to an improved structure consisting of a low proportion of the disordered cubic domain and large interslab distance of the predominant layered structure. In addition, as we know that John–teller distortion of cations, i.e.,  $\text{Ni}^{3+}$  and  $\text{Mn}^{3+}$  induce the structural changes during cycling, and also dissolution into the electrolyte after disproportion of  $\text{Mn}^{3+}$  as reaction (4) also lead to the loss of active material



Therefore, a decrease of the John–teller-sensitive cations and good crystallization are also related to the high capacity and excellent cycling performance of  $0.5\text{Li}_2\text{MnO}_3 \cdot 0.5\text{LiMn}_{0.4}\text{Ni}_{0.5}\text{Fe}_{0.1}\text{O}_2$ .

#### 4 Conclusions

$0.5\text{Li}_2\text{MnO}_3 \cdot 0.5\text{LiMn}_{0.5}\text{Ni}_{0.5}\text{O}_2$  with low Fe-doping content were synthesized via coprecipitation of carbonates and characterized by means of XRD, SEM, ICP-OES, XPS, CV, and galvanostatic charge/discharge testing. The composite structure is reasonable to understand the effect of Fe on its crystal structure and electrochemical properties. An introduction of Fe in a small amount can reduce the proportion of cubic rock-salt and broaden the interslab distance of the predominant layered structure. The favorable  $\text{Li}^+$  hopping kinetics from the microstructural and morphological point of view contributes to a high reversible capacity and good cycling stability of  $0.5\text{Li}_2\text{MnO}_3 \cdot 0.5\text{LiMn}_{0.4}\text{Ni}_{0.5}\text{Fe}_{0.1}\text{O}_2$ .

**Acknowledgments** This study was financially supported by the National 863 Program of China (No. 2009AA03Z226), the National Nature-Science Foundation of China (No. 50702007), and the Scientific Research Foundation of Beijing Excellent Doctoral Dissertation No. YB20081000801. F. Lian expresses her gratitude to

Dr. Meike Fleischhammer of ZSW for fruitful discussion on Rietveld refinement.

#### References

##### \*Self-identifying references

1. Lee DK, Park SH, Amine K, Bang HJ, Parakash J, Sun YK (2006) *J Power Sources* 162:1346
2. Ohzuku T, Nagayama M, Tsuji K, Ariyoshi K (2011) *J Mater Chem* 21:10179
3. Boulinau A, Croguennec L, Delmas C, Weill F (2009) *Chem Mater* 21:4216
4. Lu ZH, Beaulieu LY, Donaberger RA, Thomas CL, Dahn JR (2002) *J Electrochem Soc* 149:A778
5. Lim JH, Bang H, Lee KS, Amine K, Sun YK (2009) *J Power Sources* 189:571
6. Choi HJ, Lee KM, Lee JG (2001) *J Power Sources* 103:154
7. Lu ZH, Dahn JR (2003) *J Electrochem Soc* 150:A1044
8. Jain A, Singh S, Yusuf SM (2006) *Phys Rev B* 74:174419
9. Tabuchi M, Nabeshima Y, Takeuchi T, Tatsumi K, Imaizumi J, Nitta Y (2010) *J Power Sources* 195:834
10. Tabuchi M, Nabeshima Y, Shikano M, Ado K, Kageyama H, Tatsumi K (2007) *J Electrochem Soc* 154:A638
11. Kikkawa J, Akita T, Tabuchi M, Shikano M, Tatsumi K, Kohyama M (2008) *J Appl Phys* 103:104911
12. Tabuchi M, Nakashima A, Ado K, Sakaebae H, Kobayashi H, Kageyama H, Tatsumi K, Kobayashi Y, Seki S, Yamanaka A (2005) *J Power Sources* 146:287
13. Velikokhatnyi OI, Choi D, Kumta PN (2006) *Mater Sci Eng B* 128:115
14. \*Lian F, Axmann P, Stinner C, Liu QG, Wohlfahrt-Mehrens M (2008) *J Appl Electrochem* 38:613
15. Yabuuchi N, Yoshii K, Myung ST, Nakai L, Komaba S (2011) *J Am Chem Soc* 133:4404
16. Barkhouse DAR, Dahn JR (2005) *J Electrochem Soc* 152:A746
17. Shaju KM, Subba Rao GV, Chowdar BVR (2002) *Electrochim Acta* 48:145
18. Yu DYW, Yanagida K, Nakamura H, Kato Y (2009) *J Electrochem Soc* 156:A417
19. \*Yu LY, Qiu WH, Lian F, Huang JY, Kang XL (2009) *J Alloys Compd* 471:317
20. Rajakumar S, Thirunakaran R, Sivashanmugam A, Yamaki J, Gopukumar S (2009) *J Electrochem Soc* 156:246
21. Tang A, Wang X, Xu G, Zhou Z, Nie H (2009) *Mater Lett* 63:1439
22. Ni J, Zhou H, Chen J, Zhang X (2008) *Electrochim Acta* 53:3075